

Ultra-high-quality factor and ultra-high accelerating gradient achievements in a 1.3 GHz continuous wave cryomodule*

Jin-Fang Chen,¹ Yue Zong,¹ Xiao-Yun Pu,¹ Sheng-Wang Xiang,¹ Shuai Xing,¹ Zheng Li,¹ Xu-Ming Liu,¹ Yan-Fei Zhai,¹ Xiao-Wei Wu,² Yong-Zhou He,¹ Ling-Ling Gong,¹ Ji-Dong Zhang,¹ Shan-Shan Cao,¹ Wen-Ding Fang,¹ Bin-Tuan Zhang,¹ Kai Xu,¹ Yi-Bo Yu,¹ Guang-Hua Chen,¹ Li-Jun Lu,¹ Ya-Wei Huang,³ Shen-Jie Zhao,¹ Hong-Tao Hou,¹ Zhen-Yu Ma,¹ Ye-Liang Zhao,¹ Xiang Zheng,¹ Jiu-Ce Sun,³ Sen Sun,¹ Zhi-Qiang Jiang,¹ Yu-Bin Zhao,¹ Meng Zhang,¹ Ying-Bing Yan,¹ Yi-Yong Liu,¹ Qiang Gu,¹ Bo Liu,¹ Li-Xin Yin,¹ Dong Wang,¹ Hai-Xiao Deng,^{1,†} and Zhen-Tang Zhao¹

¹Shanghai Advanced Research Institute, Chinese Academy of Sciences, Shanghai 201204, China

²Zhangjiang Laboratory, Shanghai 201210, China

³ShanghaiTech University, Shanghai 201210, China

We report the world-leading performance of a 1.3 GHz cryomodule equipped with eight 9-cell superconducting radio-frequency cavities that underwent a medium-temperature furnace baking process. During continuous wave horizontal testing, these cavities achieved unprecedented average intrinsic quality factors of 4.0×10^{10} at 20 MV/m and 3.2×10^{10} at 29 MV/m, with no instances of field emission. The cryomodule demonstrates near-complete preservation of ultra-high-quality factors and ultra-high accelerating gradients from vertical to horizontal testing, marking a significant milestone in continuous-wave superconducting radio-frequency accelerator technology. This letter presents the cryomodule development experience, including cavity preparation, cryomodule assembly, degaussing, fast cooldown, and performance testing.

Keywords: SRF cryomodule· Mid-T baking· High quality factor· High accelerating gradient

I. INTRODUCTION

High Q_0 (quality factor) cryomodules equipped with superconducting radio-frequency (SRF) cavities are key components of modern accelerators, such as high-repetition X-ray FEL facilities [1], high-power extreme ultraviolet lithography light sources [2], and other future high-duty factor colliders [3]. At the Shanghai High Repetition Rate XFEL and Extreme Light Facility (SHINE) [4], more than 50 high Q_0 cryomodules operating in 1.3 GHz continuous wave (CW) mode will be installed to generate an 8 GeV electron beam. In contrast, extreme ultraviolet lithography light sources require approximately 10 high- Q_0 cryomodules operating in 1.3 GHz CW mode for a 1 GeV energy recovery linac. Generally, a high Q_0 cryomodule includes eight 9-cell TESLA cavities [5], eight fundamental power couplers (FPC), one superconducting quadrupole magnet package, and one cold beam-position monitor. The design and advancements of 1.3 GHz cryomodules are primarily attributed to the R&D efforts undertaken in large-scale facilities like the TESLA Test Facility [6], the European XFEL [7], the Linac Coherent Light Source II (LCLS-II) [8], LCLS-II HE [9] and SHINE.

Currently, nitrogen doping (N-doping) [10–14] and medium-temperature (mid-T) baking [15–17] are the two main methods used to enhance the Q_0 values of SRF cavities made of high-purity niobium. N-doping incorporates nitrogen atoms as interstitial impurities into the niobium lattice, lowering the mean free path of the RF penetration layer of

niobium, hence the BCS resistance, and reducing the residual resistance [18]. Fermilab and Jefferson Lab developed cryomodules equipped with SRF cavities treated by 2/6 N-doping recipes for LCLS-II [19, 20]. In 2023, 35 cryomodules with 2/6 N-doped cavities were commissioned for the LCLS-II, demonstrating Q_0 of 2.8×10^{10} at an average accelerating gradient of 16 MV/m in the CW operation of a superconducting linac [3]. The LCLS-II-HE cryomodule with a 2/0 N-doping recipe achieved a maximum acceleration voltage of 208 MV in CW mode, corresponding to an average accelerating gradient of 25.1 MV/m, and Q_0 of 3.0×10^{10} at a gradient of 21 MV/m [21]. Mid-T baking is a novel and simplified high- Q_0 recipe that yields results similar to those of N-doping, while preventing the formation of N_bN precipitates, which act as defects, and reducing the risk of contamination. The Institute of High Energy Physics (IHEP) developed the first high- Q_0 cryomodule equipped with eight mid-T-baked cavities, achieving Q_0 of 3.8×10^{10} at 16 MV/m and Q_0 of 3.6×10^{10} at 21 MV/m in horizontal testing [22].

At the Shanghai Advanced Research Institute (SARI), we conduct experimental cavity treatments using facilities for SRF cavity surface treatments on a platform located in Wuxi, China [23]. Both N-doped and mid-T baking recipes have been studied, achieving high accelerating gradients exceeding 25 MV/m on 1.3 GHz 9-cell cavities [24]. Since 2020, several sets of cryomodules with high- Q_0 cavities have been assembled and tested [25]. In this letter, we report the first 1.3 GHz high Q_0 cryomodule dedicated to CW operation up to 1 mA, developed at SARI. It is equipped with eight mid-T-baked cavities and eight 30 kW FPCs [26, 27], demonstrating world-leading, ultrahigh Q_0 and ultrahigh accelerating gradient performance in CW horizontal testing.

* This work was supported by Zhangjiang Laboratory, the SHINE R&D project (No. 2017SHZDZX02), the SHINE project, and the National Natural Science Foundation of China (12125508).

† Corresponding author, denghx@sari.ac.cn

60

II. MID-T BAKED CAVITIES

61 The eight cavities were mechanically fabricated by the
 62 HE-Racing Technology Company in Beijing, treated by the
 63 SHINE cavity surface treatment facilities in Wuxi [23], and
 64 tested at the SARI and IHEP vertical test (VT) stands. These
 65 cavities underwent 200 μm electropolishing, 3 h of 900 $^{\circ}\text{C}$
 66 high-temperature baking, exposure to air, and 3 h of furnace
 67 baking at 300 $^{\circ}\text{C}$ [24].

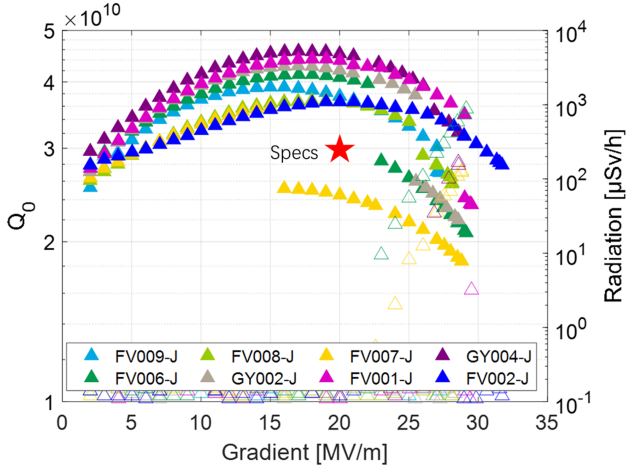
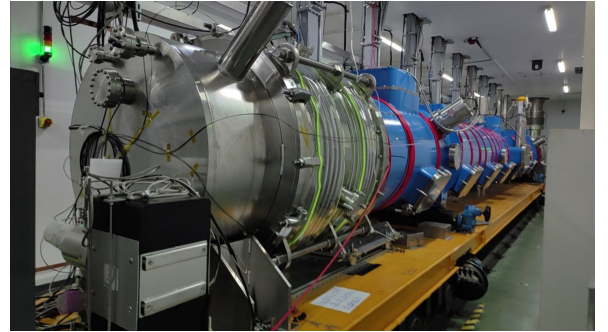


Fig. 1. Vertical test results of the eight dressed cavities. The solid triangle represents the Q_0 value, while the hollow triangle represents the radiation dose. The Q_0 values are corrected by 0.8 $\text{n}\Omega$ loss of stainless-steel flanges. The three cavities with significant radiation dose were cleaned again by high-pressure rinsing before delivery to the cryomodule assembly, without additional vertical testing.

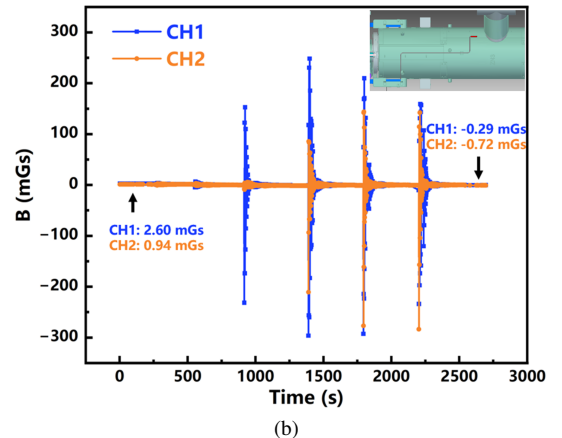


Fig. 2. Cavity string assembly in class 10 cleanroom.

68 Figure. 1 shows the vertical test results of the eight dressed
 69 cavities treated with the mid-T-baked recipe, where Q_0 is
 70 corrected by the 0.8 $\text{n}\Omega$ loss of the stainless-steel flanges.
 71 The sudden drop of Q_0 at around 16 MV/m for FV007-J, 23



(a)



(b)

Fig. 3. (a) The coils wound for cryomodule degaussing in the horizontal test stand; (b) In-situ cryomodule degaussing at room temperature before cooling down. The two flux gates are mounted at cavity 1# and 5# slots, between the two layers of magnetic shields outside the cavity helium vessel, as shown in the upper-right inset image.

72 MV/m for FV006-J, and 25 MV/m for GY002-J is attributed
 73 to flux trapping after soft quenches caused by multipacting
 74 [28], which can be recovered after warming up and perform-
 75 ing a fast cooldown. For a direct comparison between the
 76 vertical and horizontal tests, the Q_0 drop was compensat-
 77 ed for by the gap. The average Q_0 was 4.0×10^{10} at 20 MV/m,
 78 and the average maximum gradient was 29.4 MV/m. Three
 79 cavities exhibiting field emission during the vertical test were
 80 cleaned by long, high-pressure rinsing with two rounds of six
 81 turns before delivery to the cryomodule assembly. Although
 82 no further vertical tests were performed on these three cavi-
 83 ties due to the tight schedule, as shown in the horizontal test
 84 results, all field emissions were eliminated.

III. CRYOMODULE ASSEMBLY

85 The cryomodule assembly includes clean assembly of the
 86 cavity string in a class 10 cleanroom, the cold mass, and the fi-
 87 nal assembly, typically completed within approximately two
 88 months. Before string assembly, all cavities underwent an
 89 outer surface rinsing process, after which they entered the
 90 cleanroom for more thorough cleaning, including wiping the

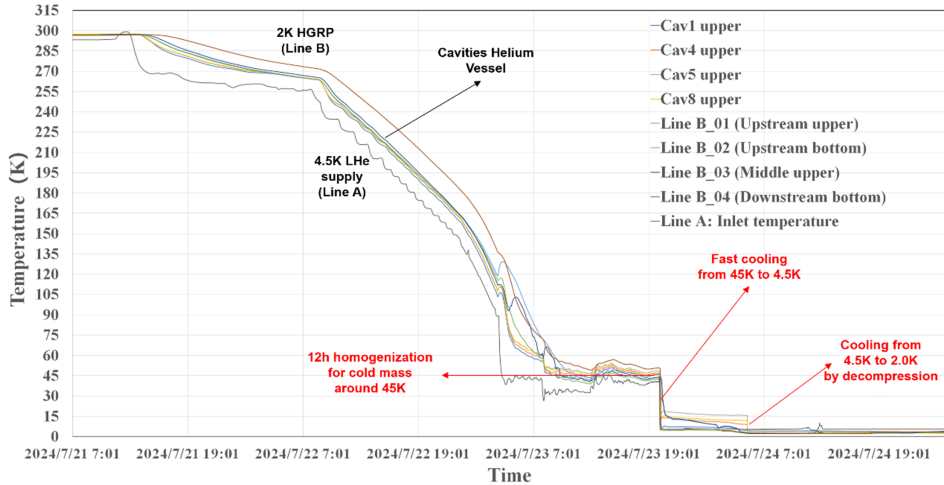


Fig. 4. Cooling curves of the SARI cryomodule from 300 K to 2 K.

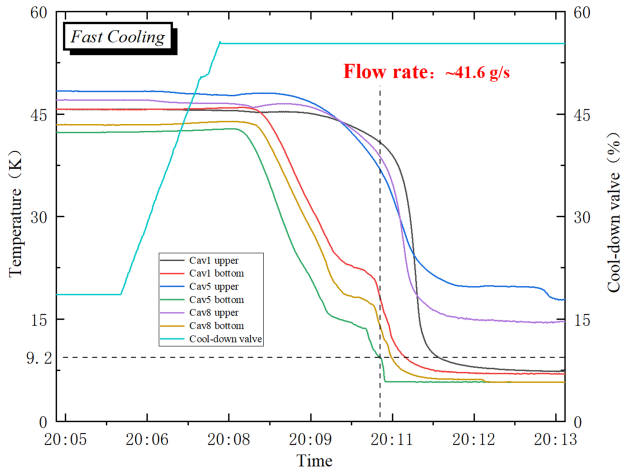


Fig. 5. Fast cooling curves for SARI cryomodule from 45 K to 4.5K.

92 outer surface, particularly the helium vessel bellows. The sur-
93 face was blown with clean nitrogen gas to verify contamina-
94 tion levels met class 10 cleanroom standards. The assem-
95 bly process began with the installation of fundamental power
96 couplers, followed by intercavity bellows from upstream to
97 downstream. Fig. 2 shows the cavity-string assembly of the
98 SARI cryomodule (CM) in a class 10 cleanroom.

99 During assembly, nitrogen gas was vented into the cavi-
100 ties at 1 slm to maintain slightly positive pressure, preventing
101 contamination from entering. Once the string assembly was
102 completed, positive-pressure leak detection was conducted to
103 identify major leaks. The cavity string was then evacuated
104 into a vacuum, followed by a second leak test under vacuum
105 conditions. Residual gas analysis assessed the cleanliness of
106 the entire cavity string. After completing these tests, the cav-
107 ity string was backfilled with nitrogen to a pressure of 1050
108 mbar, slightly higher than atmospheric pressure, for protec-
109 tion, and subsequently transported out of the cleanroom for

110 further assembly.

IV. DEGAUSSING AND COOLING DOWN

111 The cryostat was first degaussed in an east-west direction
112 at SARI. During cryomodule assembly, two flux gates were
113 mounted along the beam direction at the cavity 1# and 5#
114 slots between the two layers of magnetic shields outside the
115 cavity helium vessel. After the cryomodule was installed on
116 the horizontal test stand, the entire cryomodule was degassed
117 at room temperature, as shown in Fig. 3(a). The magnetic
118 field falls from 2.6 mGs to 0.3 mGs and from 0.9 mGs to 0.7
119 mGs after degaussing for the cavities 1# and 5#, respectively,
120 as shown in Fig. 3(b).

121 The SARI cryomodule cooling process, from 300 K to 2
122 K, follows a procedure similar to that of the European XFEL
123 [29] and LCLS-II [30], typically lasting for 3~4 days. From
124 300 K to 45 K, the average cooling rate has been controlled
125 at around 6 K/h, followed by a "stand-by mode" lasting for
126 about 12 hours to allow the entire cryomodule cold mass to
127 stabilize at the 45 K temperature level. Fast cooling from 45
128 K to 4.5 K is required for magnetic flux exclusion in high-Q
129 cavities, improving RF performance [31]. Once liquid helium
130 accumulates along the cavity string and in the two-phase pipe,
131 most of the cold mass is cooled to approximately 4.5 K. Final
132 cooling is achieved by depressurizing the saturated helium
133 vapor from around 1.2 bar to 31 mbar, reaching the operating
134 condition at 2 K superfluid helium. Fig. 4 shows the first
135 cooling step of the standard SARI cryomodule.

136 A key method to achieve high Q_0 performance at 2 K is
137 to maintain an instant liquid-helium mass flow rate, creating
138 a sufficient thermal gradient for magnetic flux expulsion as
139 the cavities pass through the superconducting transition point
140 (T_c) of approximately 9.2 K [31, 32]. Before the Q_0 test, the
141 cryomodule was warmed up to 45 K and then quickly cooled
142 again to release the magnetic flux trapped during previous

144 quenches, which reached their maximum gradient or were induced by multipacting. For the SARI cryomodule, a maximum flow rate of 41.6 g/s was achieved when the cavities passed through the T_c . Fig. 5 shows the thermal difference between the top and bottom of the dressed cavities during the horizontal test, where thermal sensors are mounted outside dressed cavities 1#, 5# and 8#.

151 V. Q_0 PERFORMANCE

152 The mass flow rate method was employed to measure the static and dynamic 2 K heat load of the cryomodule [33–35]. Fig. 6 shows the calibration results of the heat load via heaters for the SARI CM. The CM was first injected with liquid helium above half of the two-phase pipe and then evaporated in a semi-closed system (i.e., a cavity string with supply valves closed and the helium-gas-return pipe valve opened) under different heat load conditions ranging from 0 to 90 W. According to the law of conservation of energy, when dynamic balance is achieved, the helium evaporating mass flow rate, along with its latent heat (~ 23 J/g at 2 K) takes the same energy deposited on the 2 K cold mass from the outside heat load. With the above relationship between heat load and evaporating mass flow rate, a linear fit can be obtained based on the thermal heater power and flowmeter measurements. Consequently, the absolute value of the intercept point at “zero” mass flow rate gives the 2 K static heat load of the SARI cryomodule around 21.7 W, as shown in Fig. 6.

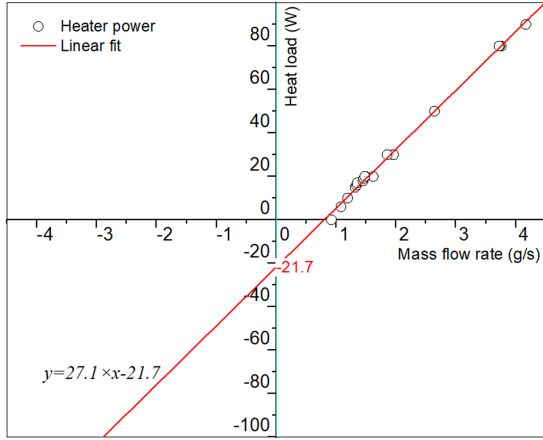


Fig. 6. Static heat load measurements for the SARI cryomodule at 2 K: the overlap of circles at 20, 30, and 80 W serves to verify the data’s repeatability and reliability.

170 The dynamic heat load of each cavity was measured by subtracting the heat load of three cavities from four cavities to improve accuracy. The estimated measurement uncertainty of Q_0 was less than 10%, and the accelerating gradient was less than 5%.

175 To directly compare Q_0 between vertical and horizontal tests, Q_0 values with a sudden drop in three cavities were compensated for by the gap at the drop gradient. Fig. 7 shows

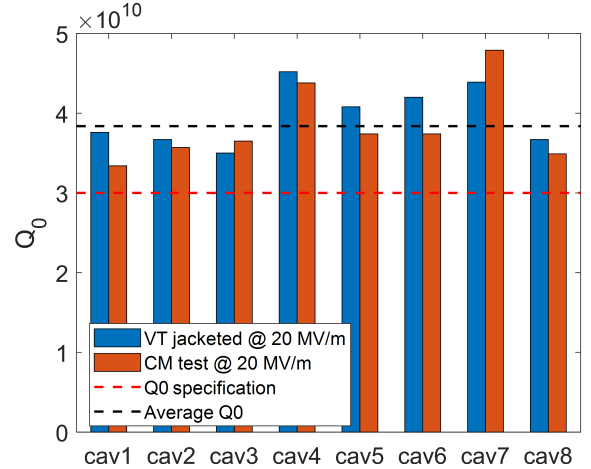


Fig. 7. Q_0 measured at 20 MV/m for each cavity in both vertical and horizontal tests. To allow direct comparison, the Q_0 values of cavities 3#, 5#, and 6# were adjusted to account for the Q_0 gap in vertical tests due to flux trapping after soft quenches.

178 a comparison of Q_0 at 20 MV/m for the eight dressed cavities 179 in both vertical and horizontal tests.

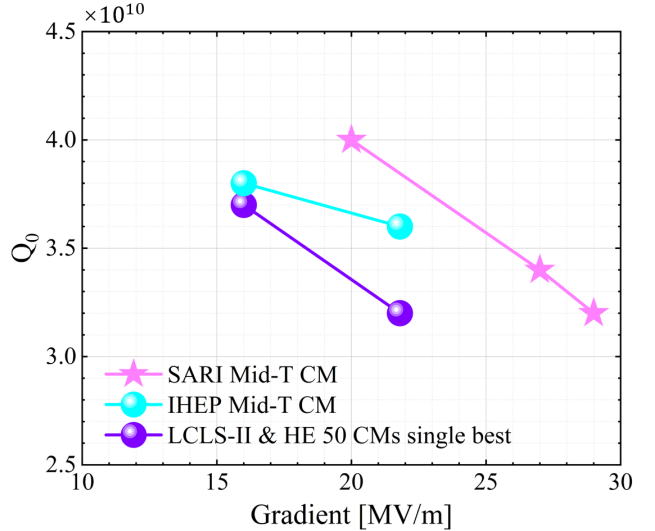


Fig. 8. Average Q_0 at 20, 27, and 29 MV/m for the SARI cryomodule in the horizontal test, compared with other top-performing cryomodules [21, 22] in the world. The administration limit for LCLS-II HE cryomodule testing is 26 MV/m for each cavity, corresponding to a maximum CM voltage of 216 MV [9].

180 The average Q_0 values at 166 MV and higher voltages in 181 CW mode were also measured for the SARI CM. The total 182 2 K heat load was 104.9 W at a total voltage of 166.1 MV 183 with all eight cavities at 20 MV/m, 194.9 W at 223.8 MV, 184 and 236.4 W at 241.3 MV, corresponding to an average Q_0 of 185 4.0×10^{10} at a gradient of 20 MV/m, 3.4×10^{10} at 27 MV/m, 186 and 3.2×10^{10} at 29 MV/m, respectively. Fig. 8 provides 187 the measurement points of the SARI CM and compares them 188 with other top cryomodules [9, 21, 22].

189

VI. GRADIENT PERFORMANCE

190 Figure 9 shows the maximum accelerating gradients for the
 191 eight dressed cavities measured in CW mode during vertical
 192 tests and in the cryomodule, where the maximum gradient is
 193 defined as stable operation for at least one minute. The usable
 194 gradient in the cryomodule is defined as meeting the condi-
 195 tions of being 0.5 MV/m less than the quench field, stable op-
 196 eration for one hour, and radiation dose less than 500 μ Sv/h
 197 measured by the G-M tube radiation detectors placed around
 198 2 m from the cryomodule in the horizontal test stand. As
 199 can be seen, all cavities approach full-gradient performance
 200 except for cavity 5#, which is limited by HOM heating, as
 201 described below.

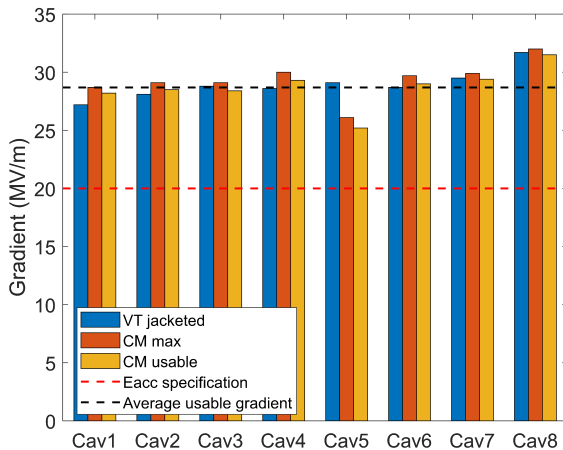


Fig. 9. Accelerating gradient measured for each jacketed-cavity in vertical and horizontal tests.

202 To accelerate a beam, long-term stable operation at the
 203 working gradient is essential for the CM. During operation,
 204 RF power can heat the FPC antennas, which are cooled
 205 through a ceramic window and CF100 flange by a 45 K in-
 206 tercept, a conduction-cooling braid connected to the 45 K
 207 helium gas pipes, eventually reaching thermal equilibrium.
 208 For the SARI CM, the temperature of each CF100 flange was
 209 monitored using thermal sensors. A stable operation test was
 210 performed at 220 MV for the SARI CM. The external Q val-
 211 ues of the eight cavities were adjusted to their optimal val-
 212 ues of approximately 6.1×10^7 for a working gradient of 20
 213 MV/m. Due to the cryogenic limit of the horizontal test stand,
 214 the eight cavities were split into two groups for stable opera-
 215 tion testing. Each cavity operated at 27.3 MV/m, except for
 216 cavity 5# at 21.7 MV/m. The group with the first four cav-
 217 ities maintained a total voltage of 113 MV, while the other
 218 group maintained 108 MV. To reduce test time, we detuned
 219 the phase of the self-excited loop to increase reflected power,
 220 thus heating the main coupler to its threshold of approxi-
 221 mately 150 K. Afterward, we tuned it back and awaited ther-
 222 mal equilibrium, or maintained it for 10 hours. Fig. 10 shows
 223 the temperature behavior of the eight FPC CF100 flanges
 224 during the 220 MV stable operation test. As shown, all the

225 temperatures of the eight CF100 flanges decreased, reaching
 226 quasi-equilibrium, with a maximum temperature of less than
 227 120 K, below the 150 K threshold. This confirms the stable
 228 operation capacity at 220 MV for this CM.

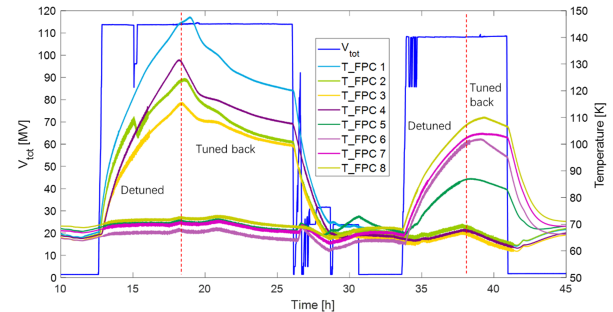


Fig. 10. Long-term stable operation test at 220 MV for SARI CM, monitoring the temperature of the FPC CF100 flanges connected to the 45 K intercept. The test was performed in two groups, with four cavities each. The phases of the self-excited loop were detuned to speed up the FPC heating to a maximum of around 150 K for FPC1, then tuned back, as shown by the turning points marked by the red dashed lines.



Fig. 11. A thermal sensor is mounted on the conducted-cooling clamp of a HOM-feedthrough copper sleeve at the cavity 5# FPC-side to monitor HOM heating

229 Table 1 summarizes the CW mode performances of the
 230 eight mid-T-baked cavities in VT and CM. The Q_0 of the en-
 231 tire CM measurement was 4.0×10^{10} at 166 MV, with all eight
 232 cavities operating simultaneously at 20 MV/m. The slight dif-
 233 ference in the average Q_0 between the individual cavities and
 234 the entire CM measurement was likely due to the uncertainty
 235 of the small heat load, as shown in Fig. 6.

236 It is worth mentioning that the cryomodule was also tested
 237 in pulsed mode with a repetition rate of 0.5 Hz and a 10%
 238 duty factor, where the total accelerating voltage reached 247.6

Table 1. Summary of individual cavity performance in the VT and cryomodule. The VT Q_0 values are corrected for stainless steel flange losses (0.8 nΩ subtracted). “*” indicates that the Q_0 was compensated for by the drop in Q_0 during the vertical test owing to flux trapping after soft quenching.

Slot in CM	SN	Vertical test		Cryomodule test			
		E_{\max} (MV/m)	$Q_0/10^{10}$ at 20 MV/m	E_{\max} (MV/m)	E_{usable} (MV/m)	FE onset (MV/m)	$Q_0/10^{10}$ at 20 MV/m
1	FV009-J	27.2	3.8	28.7	28.2	None	3.3
2	FV008-J	28.1	3.7	29.1	28.5	None	3.6
3	FV007-J	28.8	3.5*	29.1	28.4	None	3.7
4	GY004-J	28.6	4.5	30.0	29.3	None	4.4
5	FV006-J	29.1	4.1*	26.1	25.2	None	3.7
6	GY002-J	28.7	4.2*	29.7	29.0	None	3.7
7	FV001-J	29.5	4.4	29.9	29.4	None	4.8
8	FV002-J	31.7	3.7	32.0	31.5	None	3.5
Average		29.0	4.0	29.3	28.7		3.8

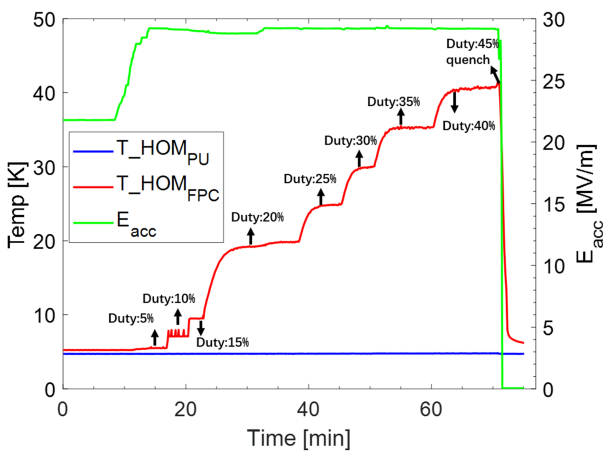


Fig. 12. Accelerating gradient of cavity 5# limited by FPC-side HOM heating, where the thermal sensors are mounted on the cooper sleeve of HOM feedthroughs.

239 MV. In this mode, cavity 5# was powered up to 29.2 MV/m,
240 the same as its maximum gradient in the vertical test. Addi-
241 tionally, no detectable field emissions were observed during
242 any of the cryomodule tests.

VII. LIMITATION FACTOR

243 When comparing the RF performances of the eight cavities
244 in the vertical and horizontal tests, cavity 5# exhibited a sig-
245 nificant decrease in the accelerating gradient. The maximum
246 CW operating gradient for cavity 5# was limited to approx-
247 imately 25.2 MV/m by quenching, accompanied by a rapid
248 temperature increase at the FPC-side HOM coupler, where
249 the thermal sensor was mounted on the copper clamp at the
250 copper sleeve of the HOM feedthrough, as shown in Fig. 11.

252 To investigate the limiting factor, we tested cavity 5# in
253 pulsed mode. With a repetition rate of 0.5 Hz and a duty
254 cycle of 5%, we began increasing the input power to the cav-

255 ity, which showed that the cavity could stably operate at 29.2
256 MV/m, similar to the maximum gradient in the vertical test,
257 with a slight temperature increase at the FPC-side HOM. We
258 then gradually increased the duty cycle in steps of 5%, while
259 maintaining a gradient of 29.2 MV/m, and a positive corre-
260 lation between the FPC-side HOM temperature and duty cycle
261 was observed. The cavity could stably operate at 29.2 MV/m
262 with a duty cycle of up to 40%, where the HOM tempera-
263 ture approached approximately 40 °C, but quenched quickly
264 once the duty cycle was increased to 45%. Fig. 12 shows
265 the relationship between the HOM temperature and the duty
266 cycle for cavity 5#. It is important to note that no field emis-
267 sions were observed during these measurements. Therefore,
268 we concluded that the limitation of cavity 5# gradient is due
269 to overheating of the HOM antenna.

VIII. CONCLUSIONS

271 A high Q_0 cryomodule equipped with eight mid-T-baked
272 1.3 GHz 9-cell cavities was assembled and tested at SARI.
273 This cryomodule achieved an ultra-high average Q_0 at the
274 operating gradients and an unprecedented total accelerating
275 voltage in CW mode. The cryomodule’s average Q_0 was
276 4.0×10^{10} at 20 MV/m and 3.2×10^{10} at 29 MV/m in the hor-
277 izontal test, which corresponds to a maximum CW RF volt-
278 age of approximately 241 MV. The RF performance of the
279 cavities was well-maintained from the vertical test to the hor-
280 izontal test. Furthermore, no field emissions were observed
281 in any of the eight cavities in the cryomodule. The success-
282 ful development of this ultra-high Q_0 and ultra-high gradient
283 cryomodule demonstrates the techniques mastered from com-
284 ponents to a completed cryomodule, marking an important
285 milestone for CW accelerator projects, such as high-repetition
286 X-ray FEL facilities, high-power extreme ultraviolet lithogra-
287 phy light sources, and other future high-duty factor colliders.

289 **Acknowledgments** The authors would like to thank all the
 290 colleagues who contributed to this work, including the SRF
 291 cryomodule, cryogenic, and general technology teams, as
 292 well as the companies and institutes that supplied the cry-
 293 omodule components and technical servers. The authors are
 294 grateful to Mi-Yi-Min Zhao and Xing-Heng Wang for the
 295 helps in figure drawing.

297 **Author Contributions** All authors contributed to and partic-
 298 ipated in the design, manufacturing, assembly, and testing of
 299 the cryomodule. Jin-Fang Chen was the cryomodule coordi-
 300 nator. Hai-Xiao Deng was the project leader. The first draft of
 301 the manuscript was written by Jin-Fang Chen, Meng Zhang,
 302 Hai-Xiao Deng and all authors commented and reviewed on
 303 previous versions and the final version of the manuscript.

304 [1] N. Huang, H. Deng, B. Liu et al., Features and futures of 353 [15] S. Posen, A. Romanenko, A. Grassellino et al., Ultra-Low Sur-
 305 X-ray free-electron lasers. *The Innovation* **2**, 100097 (2021). 354 face Resistance via Vacuum Heat Treatment of Superconduct-
 306 <https://doi.org/10.1016/j.xinn.2021.100097> 355 ing Radiofrequency Cavities. *Phys. Rev. Applied* **13**, 014024
 307 [2] N. Nakamura, R. Kato, H. Sakai et al., High-power EUV free- 356 (2019). <https://doi.org/10.1103/PhysRevApplied.13.014024>
 308 electron laser for future lithography. *Jpn. J. Appl. Phys.* **62**, 357 [16] H. Ito, H. Araki, K. Takahashi et al., Influence of Furn-
 309 SG0809 (2023). <https://doi.org/10.35848/1347-4065/acc18c> 358 ace Baking on Q-E Behavior of Superconducting Acceler-
 310 [3] J. Gao, CEPC Technical Design Report: Accelerator. 359 ating Cavities. *Prog. Theor. Exp. Phys.* **2021**, 071G01 (2021).
 311 Radiat. Detect. Technol. Methods **8**, 1–1105 (2024). 360 <https://doi.org/10.1093/ptep/ptab056>
 312 <https://doi.org/10.1007/s41605-024-00463-y> 361 [17] F. He, W. Pan, P. Sha et al., Medium-temperature furnace
 313 [4] N. Huang, Z. Liu, B. Deng et al., The MING proposal at 362 baking of 1.3 GHz 9-cell superconducting cavities at IHEP.
 314 SHINE: megahertz cavity enhanced X-ray generation. *Nucl. 363 Superconductor Science and Technology* **34**, 095005 (2021).
 315 Sci. Tech. **34**, 6 (2023). <https://doi.org/10.1007/s41365-022-01151-6> 364 <https://doi.org/10.1088/1361-6668/ac1657>
 316 [5] B. Aune, R. Bandelmann, D. Bloess et al., Superconduct- 365 [18] H. Padamsee, Superconducting Radiofrequency Tech-
 317 ing TESLA cavities. *Phys. Rev. ST Accel. Beams* **3**, 092001 366 nology for Accelerators - state of the art and emerg-
 318 (2000). <https://doi.org/10.1103/PhysRevSTAB.3.092001> 367 ing trends (WILEY-VCH GmbH, 2023.), p. 45.
 319 [6] C. Pagani, J. Weisend II, R. Bandelmann et al., Construc- 368 <https://doi.org/10.1002/9783527836314>
 320 tion, Commissioning, and Cryogenic Performances of the 369 [19] G. Wu, A. Grassellino, E. Harms et al., Achieve-
 321 First TESLA Test Facility (TTF) Cryomodule. *Advances 370 ment of Ultra-High Quality Factor in Prototype Cryo-
 322 in Cryogenic Engineering* **43**. https://doi.org/10.1007/978-1-4757-9047-4_9 371 module for LCLS-II. *arXiv:181209368*, (2018).
 323 [7] C. Madec, S. Berry, P. Charon et al., Status of E-XFEL 372 <https://doi.org/10.48550/arXiv.1812.09368>
 324 String and Cryomodule Assembly at CEA-Saclay. in *Proceedings of 373 [20] R. Legg, G. Cheng, E. Daly et al., LCLS-II Cryomodule Pro-
 325 LINAC2012*, Tel-Aviv, Israel, 2012. 374 duction at JLab. in *Proceedings of SRF2017*, Lanzhou, China,
 326 [8] T. Arkan, C. Ginsburg, Y. He et al., LCLS-II 1.3 GHz Design 375 2018.
 327 Integration for Assembly and Cryomodule Assembly Facility 376 [21] S. Posen, A. Cravatta, M. Checchin et al., High gradi-
 328 Readiness at Fermilab. in *Proceedings of SRF2015*, Whistler, 377 ent performance and quench behavior of a verification cryo-
 329 BC, 2015. 378 module for a high energy continuous wave linear ac-
 330 [9] J. Maniscalco, LCLS-II-HE cavity and cryomodule test 379 celerator. *Phys. Rev. Accel. Beams* **25**, 042001 (2022).
 331 progress. TESLA Technology Collaboration (TTC) Meeting, 380 <https://doi.org/10.1103/PhysRevAccelBeams.25.042001>
 332 [10] A. Grassellino, A. Romanenko, D. Sergatskov et al., Nitro- 381 [22] W. Pan, J. Zhai, F. He et al., High Q and high gradient per-
 333 gen and argon doping of niobium for superconducting radio 382 formance of first medium-temperature baking 1.3 GHz cryo-
 334 frequency cavities: a pathway to highly efficient accelerat- 383 module. *Phys. Rev. Accel. Beams* **27**, 092003 (2024). [doi:](https://doi.org/10.1103/PhysRevAccelBeams.27.092003)
 335 [11] A. Palczewski, Analysis Of Bcs Rf Loss Dependence On N- 384 <https://doi.org/10.1103/PhysRevAccelBeams.27.092003>
 336 doping Protocols. in *Proceedings of SRF2015*, Whistler, BC, 385 [23] J. Chen, S. Xing, J. Wu et al., Design, construction and opera-
 337 2015. 386 tion of a surface-treatment platform for SHINE superconduct-
 338 [12] D. Bafia, Optimization of High Temperature Nitrogen Doping 387 ing cavities. in *Proceedings of IPAC'24*, Nashville, TN, USA,
 339 TESLA Technology Collaboration (TTC) Meeting, 2018 388 2024.
 340 [13] Y. Zong, J. Chen, D. Wang et al., Accelerating gradi- 389 [24] Y. Zong, Q. Chen, X. Huang et al., Realization of accelerating
 341 ent improvement in nitrogen-doped superconducting 390 gradient larger than 25 MV/m on high-Q 1.3 GHz 9-cell cavities
 342 radio-frequency cavities for SHINE. *Nucl. Instrum. 391 for SHINE*. in *Proceedings of SRF2023*, Grand Rapids, MI,
 343 Methods Phys. Res. Sec. A **1057**, 168724 (2023). 392 USA, 2023.
 344 <https://doi.org/10.1016/j.nima.2023.168724> 393 [25] J. Chen, H. Hou, Z. Ma et al., Cryomodules development for
 345 [14] P. Dhakal, Nitrogen doping and infusion in SRF cav- 394 SHINE project. in *Proceedings of IPAC'24*, Nashville, TN,
 346 ities: A review. *Physics Open* **5**, 100034 (2020). 395 USA, 2024.
 347 <https://doi.org/10.1016/j.physo.2020.100034> 396 [26] Z. Ma, Lessons learned on coupler fabrication for SHINE.
 348 [397] TTC2024 Meeting, ESS Lund, Sweden, 2024.
 349 [398] Z. Ma, H. Hou, S. Zhao, et al., Manufacturing studies
 350 [399] and rf test results of the 1.3 GHz fundamental power
 351 [400] coupler prototypes. *Phys. Rev. Accel. Beams* **25**, 113501
 352 [401] (2022). <https://doi.org/10.1103/PhysRevAccelBeams.25.113501>

402 [28] D. Bafia, A. Grassellino, A. Romanenko et al., New Insights on 417
 403 Nitrogen Doping. in *Proceedings of SRF2019*, Dresden, Ger- 418
 404 many, 2019. 419

405 [29] A. Navitski, Cavities/modules test facility AMTF at DESY. 420
 406 *Americas Workshop on Linear Colliders 2014*, Fermilab, 2014. 421

407 [30] G. Wu, E. Harms, A. Grassellino et al., Performance of the 422
 408 high Q CW prototype cryomodule for LCLS-II at FNAL. in 423
 409 *Proceedings of SRF2017*, Lanzhou, China, 2017. 424

410 [31] S. Posen, G. Wu, A. Grassellino et al., Role of magnetic 425
 411 flux expulsion to reach $Q_0 > 3 \times 10^{10}$ in superconducting 426
 412 rf cryomodules. *Phys. Rev. Accel. Beams* **22**, 032001 (2019). 427
 413 <https://doi.org/10.1103/PhysRevAccelBeams.22.032001> 428

414 [32] D. Gonnella, R. Eichhorn, F. Furuta et al, Nitrogen- 429
 415 doped 9-cell cavity performance in a test cryomod- 430
 416 ule for LCLS-II. *J. Appl. Phys.* **117**, 023908 (2015). 431

417 [33] X. Wang, S. Barbanotti, J. Eschke et al., Thermal per- 418
 419 formance analysis and measurements of the prototype cry- 420
 421 omodules of European XFEL accelerator—Part II. *Nucl. In- 422
 423 strum. Methods Phys. Res. Sec. A* **763**, 688-700 (2014). 424
 425 <https://doi.org/10.1016/j.nima.2014.07.045> 426

427 [34] E. Harms, LCLS-II cryomodule heat load measurements at 428
 429 Fermilab. *TESLA Technology Collaboration (TTC) Meeting*, 2021. 430

426 [35] W. Pan, R. Ge, M. Li et al., Cryogenic system of the high per- 427
 428 formance 1.3 GHz 9-cell superconducting radio frequency pro- 429
 430 totype cryomodule. *Applied Thermal Engineering* **255**, 124042 431
 432 (2024). <https://doi.org/10.1016/j.applthermaleng.2024.124042> 433